Phase space structure for matched intense charged-particle beams in periodic focusing transport systems

Chiping Chen[a] and Renato Pakter
Plasma Science and Fusion Center, Massachusetts Institute of Technology, Cambridge, Massachusetts 02139

Ronald C. Davidson
Plasma Physics Laboratory, Princeton University, Princeton, New Jersey 08543

(Received 11 May 1999; accepted 15 June 1999)

Test particle motion is analyzed analytically and numerically in the field configuration consisting of the equilibrium self-electric and self-magnetic fields of a well-matched, thin, continuous, intense charged-particle beam and an applied periodic focusing solenoidal magnetic field. The self fields are determined self-consistently, assuming the beam to have a uniform-density, rigid-rotor Vlasov equilibrium distribution. Using the Hamilton–Jacobi method, the betatron oscillations of test particles in the average self fields and applied focusing field are analyzed, and the nonlinear resonances induced by periodic modulations in the self fields and applied field are determined. The Poincaré surface-of-section method is used to analyze numerically the phase-space structure for test particle motion outside the outermost envelope of the beam over a wide range of system parameters. For vacuum phase advance $\sigma_v = 80°$, it is found that the phase-space structure is almost entirely regular at low beam intensity (phase advance $\sigma \gtrsim 70°$, say), whereas at moderate beam intensity ($30° \lesssim \sigma \lesssim 70°$), nonlinear resonances appear, the most pronounced of which is the third-order primary nonlinear resonance. As the beam intensity is further increased ($\sigma \lesssim 30°$), the widths of the higher-order nonlinear resonances increase, and the chaotic region of phase space increases in size. Furthermore, the many chaotic layers associated with the separatrices of the primary and secondary nonlinear resonances are still divided by the remaining invariant Kolmogorov–Arnold–Moser surfaces, even at very high beam intensities. The implications of the rich nonlinear resonance structure and chaotic particle motion found in the present test-particle studies are discussed in the context of halo formation. © *1999 American Institute of Physics.* [S1070-664X(99)03409-6]

I. INTRODUCTION

Halo formation and control in intense charged-particle beams has been the subject of recent vigorous theoretical, computational, and experimental investigations.[1–20] It is of fundamental importance in the development of next-generation high-intensity accelerators for basic scientific research in high-energy and nuclear physics, as well as for a wide variety of applications ranging from heavy ion fusion, accelerator production of tritium, accelerator transmutation of nuclear waste, spallation neutron sources, and high-power free-electron lasers. In these high-intensity accelerators, beam halos must be controlled in order to minimize beam losses and activation of the accelerator structure.

It is well known that a space-charge-dominated beam can develop a sizable halo if there is a root-mean-square (rms) mismatch between the beam and the transport system.[2–4,6,10–12] The mechanism for halo formation in rms-mismatched beams has been well developed in the particle-core model.[3,6] When there is a sizable mismatch, the halo can contain a substantial fraction (up to 15%) of the entire beam.

Recently, it has been shown theoretically[5,9,15,16] that in periodic focusing transport systems, radial nonuniformities in charge density in rms-matched space-charged-dominated beams can also cause halo formation. The mechanism of halo formation in rms-matched beams has been identified with chaotic particle motion[21] and nonlinear resonances occurring in the vicinity of the boundary of phase space occupied by the particles in the beam core. Invariant Kolmogorov–Arnold–Moser (KAM) surfaces[21] play an important role in confining halo particles transverse to the direction of beam propagation.

The purpose of this paper is to analyze the dynamics of test particles in the field configuration consisting of the equilibrium self-electric and self-magnetic fields of a well-matched, thin, continuous, intense charged-particle beam and an applied periodic focusing solenoidal magnetic field. Unlike previous studies of halo formation in rms-mismatched beams and rms-matched beams with nonuniformities in charge density,[1–20] this paper addresses the fundamental question of how the phase-space structure varies with beam intensity, focusing field strength and beam rotation under the best conditions corresponding to a matched equilibrium beam. Therefore, in the present analysis, the self fields[22] are determined self-consistently, assuming the beam to have a uniform-density rigid-rotor Vlasov equilibrium distribution[23,24] which includes the well-known Kapchinskij–Vladirmirskij (KV) beam equilibrium distribution[25] as a special case. Using the Hamilton–Jacobi method, the betatron oscillations of test particles in the aver-

[a]Electronic mail: chenc@psfc.mit.edu

 © 1999 American Institute of Physics

Downloaded 30 Aug 2001 to 192.55.106.156. Redistribution subject to AIP license or copyright, see http://ojps.aip.org/pop/popcr.jsp

age self fields and applied field are analyzed, and the nonlinear resonances induced by periodic modulations in the self fields and applied field are determined. The Poincaré surface-of-section method[21] is used to analyze the phase-space structure for test particle motion outside the outermost envelope of the beam over a wide range of system parameters. It is found that the phase-space structure changes significantly as the canonical angular momentum (P_θ), beam intensity (as measured by SK/ε_T or σ/σ_v), vacuum phase advance σ_v, or beam rotation (ω_b) is varied. The implications of the rich nonlinear resonance structure and chaotic particle motion found in the present test-particle studies are discussed in the context of halo formation. By examining the intrinsic properties of phase space of test particle motion outside of a perfectly matched beam as a function of beam intensity, focusing field strength and beam rotation, we gain valuable insights as to which operating regimes are more or less robust against the ejection of halo particles from the beam under small beam mismatch and/or collective excitations in the beam core.

To briefly summarize, based on a comprehensive study of the phase-space structure for test-particle motion for vacuum phase advance $\sigma_v = 80°$, we find that the phase-space structure is almost entirely regular at low beam intensity (phase advance $\sigma \gtrsim 70°$, say), whereas at moderate beam intensity ($30° \lesssim \sigma \lesssim 70°$), nonlinear resonances appear, the most pronounced of which is the third-order primary nonlinear resonance. As the beam intensity is further increased ($\sigma \lesssim 30°$), the widths of the higher-order nonlinear resonances increase, and the chaotic region of phase space increases in size. Furthermore, the many chaotic layers associated with the separatrices of the primary and secondary nonlinear resonances are still divided by the remaining invariant KAM surfaces, even at very high beam intensities. Therefore, in the context of the present test-particle analysis, chaotic layers do *not* form an extended chaotic region in phase space. In actual beam propagation experiments, however, it is expected that sufficient beam mismatch or perturbations about the periodically focused beam equilibrium can cause the particles to cross the invariant surfaces and form a halo.

The organization of this paper is as follows. After a discussion of the theoretical model and assumptions in Sec. II, the betatron oscillations and nonlinear resonances are analyzed using the Hamilton–Jacobi method in Sec. III. The phase-space structure of test particle motion over hundreds of lattice periods is examined numerically in Sec. IV. Conclusions are given in Sec. V.

II. THEORETICAL MODEL AND ASSUMPTIONS

In the present analysis, we consider a thin, continuous, intense charged-particle beam propagating in the z direction with characteristic axial velocity $\beta_b c$ and kinematic energy $\gamma_b mc^2$ through the periodic focusing solenoidal magnetic field

$$\mathbf{B}^{\mathrm{sol}}(\mathbf{x}) = B_z(s)\mathbf{e}_z - \tfrac{1}{2}B_z'(s)(x\mathbf{e}_x + y\mathbf{e}_y). \tag{1}$$

Here, $\mathbf{e}_x$ and $\mathbf{e}_y$ are unit Cartesian vectors perpendicular to the beam propagation direction, $s=z$ is the axial coordinate, $x\mathbf{e}_x + y\mathbf{e}_y$ is the transverse displacement from the beam axis at $(x,y)=(0,0)$, the superscript ''prime'' denotes d/ds with $B_z'(s) = dB_z(s)/ds$, and the axial component of magnetic field satisfies

$$B_z(s+S) = B_z(s), \tag{2}$$

where S is the axial period of the focusing field.

To determine the self-electric and self-magnetic fields[22] consistently, we make the following assumptions: (a) the Budker parameter $\nu = N_b q^2/mc^2$ for the beam is small compared with γ_b; (b) the axial momentum spread of the beam particles is small in comparison with $\gamma_b m\beta_b c$; (c) the beam is axisymmetric ($\partial/\partial\theta = 0$); and (d) the beam is perfectly matched into the focusing field with uniform density profile over the beam cross section,

$$n_b(r,s) = \begin{cases} N_b/\pi r_b^2(s), & 0 \leqslant r < r_b(s) \\ 0, & r > r_b(s). \end{cases} \tag{3}$$

In Eq. (3), $r = (x^2+y^2)^{1/2}$ is the radial coordinate, $r_b(s) = r_b(s+S)$ is the outer envelope of the beam, and $N_b = 2\pi\int_0^\infty n_b r\,dr = \text{const.}$ is the number of particles per unit axial length. The periodic outer beam envelope $r_b(s) = r_b(s+S)$ corresponds to a special solution of the beam envelope equation[23,24]

$$\frac{d^2 r_b}{ds^2} + \kappa_s(s) r_b - \frac{K}{r_b} - \frac{\varepsilon_T^2}{r_b^3} = 0, \tag{4}$$

where $K = 2q^2 N_b/\gamma_b^3\beta_b^2 mc^2$ is the normalized perveance, $\kappa_z(s) = [qB_z(s)/2\gamma_b\beta_b mc^2]^2 = [\Omega_c(s)/2\beta_b c]^2$ is the focusing parameter, $\varepsilon_T =$ const. is the total unnormalized emittance, q and m are the particle charge and rest mass, respectively, and c is the speed of light *in vacuo*. The transverse phase-space distribution that self-consistently generates the density profile in Eq. (3) is discussed in the Appendix.

Consistent with the thin-beam assumption ($r_b \ll S$), the scalar potential for the self-electric field $\mathbf{E}^s = -\nabla\phi^s$ is determined from

$$\frac{1}{r}\frac{\partial}{\partial r} r \frac{\partial \phi^s}{\partial r} = -4\pi q n_b(r,s), \tag{5}$$

where use has been made of the approximation $\nabla^2 \cong \nabla_\perp^2$. Integrating Eq. (5) for the density profile in Eq. (3), and applying the boundary condition $\phi^s(r=r_w,s)=0$ at the wall of a perfectly conducting cylindrical tube with constant radius r_w yields

$$\phi^s(r,s) = \begin{cases} qN_b(1 - r^2/r_b^2) + 2qN_b \ln(r_w/r_b), & 0 \leqslant r < r_b(s) \\ 2qN_b \ln(r_w/r), & r_b(s) < r \leqslant r_w. \end{cases} \tag{6}$$

Because the axial momentum spread is assumed to be negligibly small, the vector potential for the self-magnetic field $\mathbf{B}^s = \nabla\times(A_z^s\mathbf{e}_z)$ is given approximately by

$$A_z^s(r,s) = \beta_b \phi^s(r,s), \tag{7}$$

Downloaded 30 Aug 2001 to 192.55.106.156. Redistribution subject to AIP license or copyright, see http://ojps.aip.org/pop/popcr.jsp

where $\beta_b c$ is the characteristic axial velocity of the beam.

In the analysis of the particle motion, it is convenient to transform to the Larmor frame[26] which rotates with angular velocity $d\theta_L/ds = -\sqrt{\kappa_z(s)} = -qB_z(s)/2\gamma_b\beta_b mc^2$ relative to the laboratory frame, i.e.,

$$\tilde{x}(s) = x(s)\cos[\theta_L(s)] + y(s)\sin[\theta_L(s)], \tag{8}$$

$$\tilde{y}(s) = -x(s)\sin[\theta_L(s)] + y(s)\cos[\theta_L(s)]. \tag{9}$$

In cylindrical coordinates $(\tilde{r},\tilde{\theta})$ in the Larmor frame, the equations of motion transverse to the direction of beam propagation can be derived from the normalized Hamiltonian

$$\tilde{H}_\perp(\tilde{r},\tilde{P}_r,\tilde{P}_\theta,s) = \frac{1}{2}\left(\tilde{P}_r^2 + \frac{\tilde{P}_\theta^2}{\tilde{r}^2}\right) + \frac{1}{2}\kappa_z(s)\tilde{r}^2 + \psi(\tilde{r},s), \tag{10}$$

where the normalized self-field potential $\psi(\tilde{r},s)$ is defined by

$$\psi(\tilde{r},s) = \frac{q}{\gamma_b^3 m\beta_b^2 c^2}\phi^s(\tilde{r},s) = \begin{cases} (K/2)[1-\tilde{r}^2/r_b^2(s)] + K\ln[r_w/r_b(s)], \\ \quad 0 \leq \tilde{r} < r_b(s) \\ K\ln[r_w/\tilde{r}], \quad r_b(s) < \tilde{r} \leq r_w. \end{cases} \tag{11}$$

From Eq. (10), the equations of motion can expressed as

$$\frac{d\tilde{r}}{ds} = \frac{\partial}{\partial\tilde{P}_r}\tilde{H}_\perp = \tilde{P}_r, \tag{12}$$

$$\frac{d\tilde{\theta}}{ds} = \frac{\partial}{\partial\tilde{P}_\theta}\tilde{H}_\perp = \frac{\tilde{P}_\theta}{\tilde{r}^2}, \tag{13}$$

$$\frac{d\tilde{P}_r}{ds} = -\frac{\partial}{\partial\tilde{r}}\tilde{H}_\perp = \frac{\tilde{P}_\theta^2}{\tilde{r}^3} - \kappa_z(s)\tilde{r} - \frac{\partial}{\partial\tilde{r}}\psi(\tilde{r},s), \tag{14}$$

$$\frac{d\tilde{P}_\theta}{ds} = -\frac{\partial}{\partial\tilde{\theta}}\tilde{H}_\perp = 0. \tag{15}$$

It follows from Eq. (15) that the canonical angular momentum is conserved, i.e.,

$$\tilde{P}_\theta = \tilde{x}\tilde{P}_y - \tilde{y}\tilde{P}_x = \text{const.}, \tag{16}$$

which is expected for axisymmetric beam propagation. Combining Eqs. (12) and (14) yields

$$\frac{d^2\tilde{r}}{ds^2} + \kappa_z(s)\tilde{r} - \frac{\tilde{P}_\theta^2}{\tilde{r}^3} + \frac{\partial}{\partial\tilde{r}}\psi(\tilde{r},s) = 0. \tag{17}$$

For a particle in the beam interior ($\tilde{r} < r_b$), the equation of motion (17) is integrable. For a particle outside the beam ($\tilde{r} > r_b$), the equation of motion is generally *nonintegrable*[21] because of the nonlinear dependence of $\partial\psi/\partial\tilde{r}$ on the radial coordinate $\tilde{r}$.

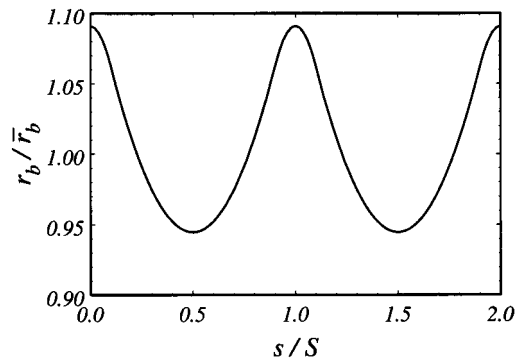

FIG. 1. Plot of the normalized beam radius $r_b(s)/\bar{r}_b$ vs normalized propagation distance s/S for intense beam propagation through a periodic step-function lattice. Here, $r_w/\bar{r}_b = 5$ is assumed, and the choice of system parameters corresponds to: $\eta = 0.2$, $S^2\hat{\kappa}_z = 6.5$, and $SK/\varepsilon_T = 4.0$.

III. ANALYSIS OF NONLINEAR RESONANCES

In this section, we analyze the nonlinear resonances in the particle motion in the Larmor frame described by Eq. (17). To simplify the notation, we omit the ''tilde'' in Larmor frame variables in the remainder of this paper. For present purposes, the Hamiltonian in Eq. (10) is expressed as

$$H_\perp(r,P_r,P_\theta,s) = H_0(r,P_r,P_\theta) + H_1(r,P_r,P_\theta,s), \tag{18}$$

where

$$H_0(r,P_r,P_\theta) = \tfrac{1}{2}P_r^2 + V_0(r,P_\theta) \equiv \frac{1}{2}P_r^2 + \frac{1}{2}\bar{\kappa}_z r^2 + \frac{P_\theta^2}{2r^2} + \psi(r,s)|_{r_b(s)=\bar{r}_b}, \tag{19}$$

$$H_1(r,P_r,P_\theta,s) = \tfrac{1}{2}[\kappa_z(s) - \bar{\kappa}_z]r^2 + \psi(r,s) - \psi(r,s)|_{r_b(s)=\bar{r}_b}. \tag{20}$$

In Eqs. (18)–(20), $\psi(r,s)$ is defined in Eq. (11), and the effective mean beam radius $\bar{r}_b$ is defined by

$$\bar{r}_b = \left(\frac{\varepsilon_T S}{\sigma}\right)^{1/2}, \tag{21}$$

where $\sigma = \varepsilon_T\int_s^{s+S} ds/r_b^2(s)$ is the space-charge-depressed phase advance for the rigid-rotor Vlasov equilibrium. The effective mean focusing parameter $\bar{\kappa}_z$ occurring in Eqs. (19) and (20) is defined by

$$\bar{\kappa}_z = \frac{K}{\bar{r}_b^2} + \frac{\varepsilon_T^2}{\bar{r}_b^4}. \tag{22}$$

Physically, the Hamiltonian H_0 provides a good approximate description of the (slow) betatron oscillations, whereas the perturbation H_1 describes nonlinear resonances induced by the (fast) oscillations in $\kappa_z(s)$ and $r_b(s)$.

For future references, Fig. 1 shows a plot of the normalized beam radius $r_b(s)/\bar{r}_b$ versus normalized propagation distance s/S, obtained numerically by integrating the beam envelope equation (4) for intense beam propagation through a periodic step-function lattice with

Downloaded 30 Aug 2001 to 192.55.106.156. Redistribution subject to AIP license or copyright, see http://ojps.aip.org/pop/popcr.jsp

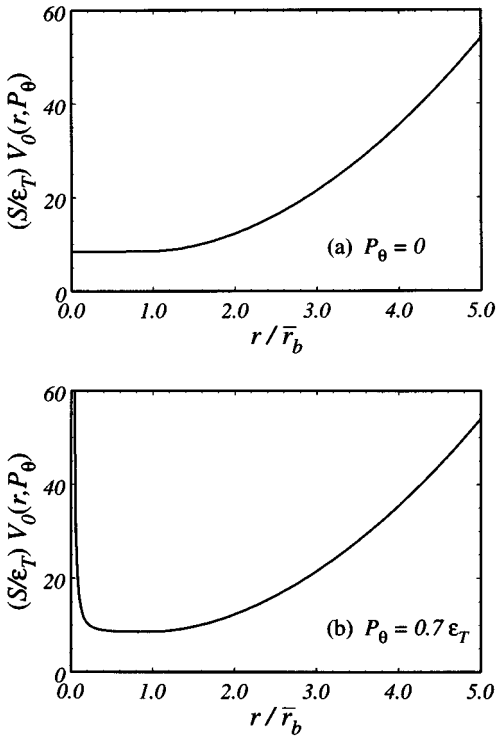

FIG. 2. Plots of the normalized effective potential $(S/\varepsilon_T)V_0(r,P_\theta)$ [Eq. (19)] vs normalized radial coordinate $r/\overline{r_b}$ for intense beam propagation through a periodic step-function lattice. Here, $r_w/\overline{r_b}=5$ is assumed, and the two cases correspond to the choices of system parameters: (a) $\eta=0.2$, $S^2\hat{\kappa}_z=6.5$, $SK/\varepsilon_T=4.0$, and $P_\theta/\varepsilon_T=0$, and (b) $\eta=0.2$, $S^2\hat{\kappa}_z=6.5$, $SK/\varepsilon_T=4.0$, and $P_\theta/\varepsilon_T=0.7$. For both cases, the vacuum and space-charge-depressed phase advances are $\sigma_v=68°$ and $\sigma=18.6°$, respectively.

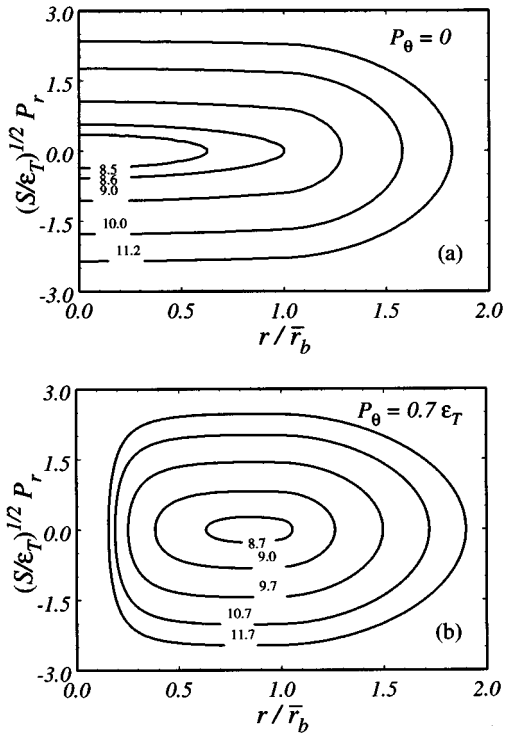

FIG. 3. Plots of constant-H_0 contours for several values of $(S/\varepsilon_T)H_0$ as labeled in the phase space (r,P_r) for the same choices of system parameters as in Figs. 2(a) and 2(b), respectively.

$$\kappa_z(s)=\begin{cases}\hat{\kappa}_z, & 0\leqslant s<\eta S/2\\ 0, & \eta S/2\leqslant s<S-\eta S/2\\ \hat{\kappa}_z, & S-\eta S/2\leqslant s<S.\end{cases}\tag{23}$$

Here, $\hat{\kappa}_z=\text{const.}$, $\kappa_z(s+S)=\kappa_z(s)$, and η is the so-called filling factor for the lattice. In Fig. 1, $r_w/\overline{r_b}=5$ is assumed, and the choice of system parameters corresponds to: $\eta=0.2$, $S^2\hat{\kappa}_z=6.5$, $SK/\varepsilon_T=4.0$. The vacuum and space-charge-depressed phase advances are found to be $\sigma_v=\varepsilon_T\int_s^{s+S}ds/r_b^2(s)|_{K=0}=68°$ and $\sigma=\varepsilon_T\int_s^{s+S}ds/r_b^2(s)=18.6°$, respectively.

A. Betatron oscillation frequency

Because P_θ is a constant of the motion and H_0 is independent of s, the unperturbed motion described by the Hamiltonian H_0 is integrable. Figure 2 shows a plot of the normalized effective potential $(S/\varepsilon_T)V_0(r,P_\theta)$ versus normalized radial coordinate $r/\overline{r_b}$ for intense beam propagation through the periodic step-function lattice defined in Eq. (23). In Fig. 2, $r_w/\overline{r_b}=5$ is assumed, and the two cases correspond to the following choices of system parameters: (a) $\eta=0.2$, $S^2\hat{\kappa}_z=6.5$, $SK/\varepsilon_T=4.0$, and $P_\theta/\varepsilon_T=0$; and (b) $\eta=0.2$, $S^2\hat{\kappa}_z=6.5$, $SK/\varepsilon_T=4.0$, and $P_\theta/\varepsilon_T=0.7$. For both cases shown in Fig. 2, the vacuum and space-charge-depressed phase advances are given by $\sigma_v=\varepsilon_T\int_s^{s+S}ds/r_b^2(s)|_{K=0}=68°$ and $\sigma=\varepsilon_T\int_s^{s+S}ds/r_b^2(s)=18.6°$, respectively. As illustrated in Fig. 2, the effective potential $V_0(r,P_\theta)$ has a minimum at $r=r_0$, where r_0 is defined by

$$\frac{r_0^2}{\overline{r_b^2}}=\begin{cases}|P_\theta|/\varepsilon_T, & |P_\theta|<\varepsilon_T\\ [K+(K^2+4\overline{\kappa_z}P_\theta^2)^{1/2}]/[K+(K^2+4\overline{\kappa_z}\varepsilon_T^2)^{1/2}], & |P_\theta|>\varepsilon_T.\end{cases}\tag{24}$$

In Fig. 3, constant-H_0 contours are plotted in the phase space (r,P_r) for several values of $(S/\varepsilon_T)H_0$, and the same choices of system parameters as in Fig. 2. For $P_\theta/\varepsilon_T=0.7$ and specified value of H_0, the particle undergoes betatron oscillations about $r=r_0$, corresponding to motion on constant-H_0 contours in the phase space (r,P_r) as shown in Fig. 3(b). In general, the betatron oscillation frequency depends on the amplitude of the oscillations.

To determine the betatron oscillation frequency, we employ the Hamilton–Jacobi method[27] and perform a canonical transformation from (r,P_r) to the action-angle variables (ϕ,J). Let $W(r,J)$ be the characteristic function satisfying the partial differential equation

$$\frac{1}{2}\left(\frac{\partial W}{\partial r}\right)^2+V_0(r,P_\theta)=H_0=\text{const.}\tag{25}$$

As discussed below, the dependence of W on J is uniquely determined because of the one-to-one correspondence between H_0 and J [see Eq. (29)]. A formal expression for the angle variable ϕ is given by

Downloaded 30 Aug 2001 to 192.55.106.156. Redistribution subject to AIP license or copyright, see http://ojps.aip.org/pop/popcr.jsp

$$\phi=\frac{\partial W}{\partial J}. \tag{26}$$

The action variable J can be expressed as

$$J=\frac{1}{2\pi}\oint P_r\,dr=\frac{1}{\pi}\int_{r_-}^{r_+}\{2[H_0-V_0(r,P_\theta)]\}^{1/2}\,dr, \tag{27}$$

where the turning points $r_\pm$ solve the algebraic equation

$$H_0=V_0(r_\pm,P_\theta), \tag{28}$$

and $r_+>r_-$ is assumed. Because the action variable J increases monotonically with increasing H_0, Eq. (27) can be inverted to yield a Hamiltonian of the form

$$H_0=H_0(J,P_\theta). \tag{29}$$

The betatron oscillation frequency can then be expressed as

$$\omega_\beta(J,P_\theta)=\frac{\partial H_0}{\partial J}, \tag{30}$$

which, in general, must be evaluated numerically. Before presenting numerical results, we discuss two special cases.

For particle motion inside the mean beam envelope with $r_+<\overline{r_b}$, it is readily shown from Eq. (27) that the action variable can be expressed as

$$J=\frac{SH_0}{2\sigma}+\frac{P_\theta}{2}, \tag{31}$$

where use has been made of Eqs. (21) and (22). It follows from Eqs. (30) and (31) that the betatron oscillation frequency is given by

$$\omega_\beta=\frac{\partial H_0}{\partial J}=\frac{2\sigma}{S}, \tag{32}$$

which is independent of the amplitude, as expected for particle motion in the beam interior. Note that the factor of 2 in Eq. (32) arises from the fact that in the present description of the betatron oscillations, the radial coordinate $r=(x^2+y^2)^{1/2}$ is used as a generalized coordinate, instead of a Cartesian coordinate, say x.

As the outer oscillation amplitude r_+ increases well beyond the mean beam envelope $(\overline{r_b})$, the oscillation frequency increases because the influence of space charge on the betatron oscillations become less pronounced. In the limit where $r_+\gg\overline{r_b}$, the betatron frequency is given by

$$\omega_\beta=\frac{2\sigma_v}{S}, \tag{33}$$

where $\sigma_v=\varepsilon_T\int_s^{s+S}ds/r_b^2(s)|_{K=0}$ is the vacuum phase advance.

Figure 4 shows a plot of the betatron oscillation frequency ω_β versus normalized betatron oscillation amplitude $(r_+-r_0)/r_0$ for the same choices of system parameters as in Figs. 2 and 3.

B. Nonlinear resonances

Under the influence of the perturbation H_1, a variety of nonlinear resonances occur due to the coupling of the (slow) betatron oscillations and the (fast) oscillations in the focusing parameter $\kappa_z(s)$ and associated modulation in the beam envelope $r_b(s)$. The locations and widths of the nonlinear resonances are analyzed in this section.

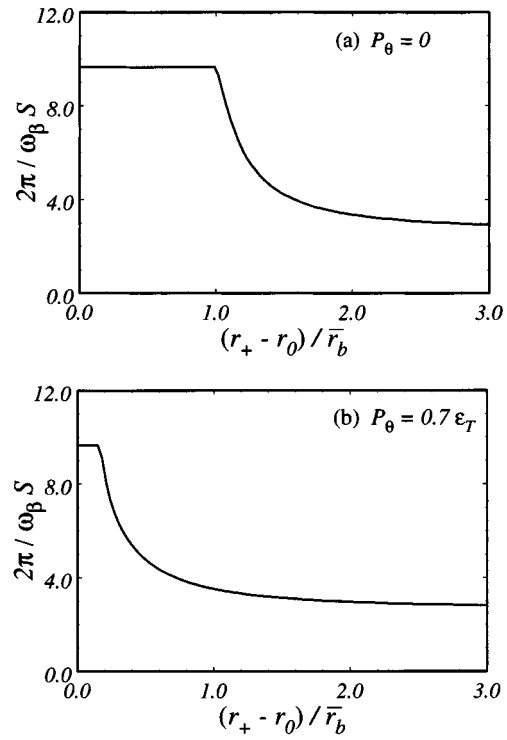

FIG. 4. Plots of the normalized betatron oscillation period $2\pi/\omega_\beta S$ [Eq. (30)] vs normalized betatron oscillation amplitude $(r_+-r_0)/\overline{r_b}$ for the same choices of system parameters as in Figs. 2(a) and 2(b), respectively.

Making use of the action-angle variables (ϕ,J) discussed in Sec. III A, we express the total Hamiltonian H formally as

$$H(\phi,J,P_\theta,s)=H_0(J,P_\theta)+H_1(\phi,J,s). \tag{34}$$

Expanding H_1 in a Fourier series representation in ϕ and s, we obtain

$$H_1=\sum_{n=-\infty}^{\infty}\sum_{l=-\infty}^{\infty}a_{nl}(J)\exp[i(n\phi+2l\pi s/S)], \tag{35}$$

where the Fourier coefficients $a_{nl}(J)$ are given by

$$a_{nl}(J)=\frac{1}{2\pi S}\int_0^S ds\int_0^{2\pi}d\phi H_1(J,\phi,s)\times\exp[-i(n\phi+2l\pi s/S)]. \tag{36}$$

A nonlinear resonance occurs when the resonance condition

$$n\frac{d\phi}{ds}+\frac{2l\pi}{S}\cong n\omega_\beta(J,P_\theta)+\frac{2l\pi}{S}=0 \tag{37}$$

is satisfied. Of particular interest in the present analysis are the primary nonlinear resonances with $l=-1$ that satisfy the resonance condition

Downloaded 30 Aug 2001 to 192.55.106.156. Redistribution subject to AIP license or copyright, see http://ojps.aip.org/pop/popcr.jsp

$$n\omega_\beta(J_n,P_\theta)=\frac{2\pi}{S}, \tag{38}$$

where J_n determines the location of the primary resonance of order n in the phase space (ϕ,J), i.e., at $J=J_n$.

To estimate the width of the nth-order primary resonance, we retain a single resonance term in the Fourier series in Eq. (20) and express the Hamiltonian approximately as

$$H(\phi,J,P_\theta,s) \cong H_0(J,P_\theta)+2|a_{n,-1}(J)|\cos(n\phi-2\pi s/S+\alpha_{n,-1}). \tag{39}$$

Here, $\alpha_{n,-1}(J)$ is the argument of the complex Fourier coefficient $a_{n,-1}$, and use has been made of $a_{n,-1}=|a_{n,-1}|\exp(i\alpha_{n,-1})=a^*_{-n,1}$. Expanding $H_0(J)$ about $J=J_n$, the Hamiltonian in Eq. (39) can be approximated by

$$\begin{aligned}H(\phi,J,P_\theta,s)\cong{}& H_0(J_n,P_\theta)+\omega_\beta(J_n,P_\theta)(J-J_n)\\ &+\frac{1}{2}\frac{\partial}{\partial J}\omega_\beta(J,P_\theta)|_{J=J_n}(J-J_n)^2\\ &+2|a_{n,-1}(J_n)|\cos(n\phi-2\pi s/S\\ &+\alpha_{n,-1}).\end{aligned} \tag{40}$$

Performing a canonical transformation with $\phi-2\pi s/nS+\alpha_{n,-1}/n\rightarrow\phi$ and $H\rightarrow H-2\pi J/nS$, the Hamiltonian in Eq. (40) becomes

$$\begin{aligned}H(\phi,J,P_\theta,s)={}&\frac{1}{2}\left(\frac{\partial\omega_\beta}{\partial J}\right)_{J=J_n}(\delta J)^2\\ &+2|a_{n,-1}(J_n)|\cos(n\phi)+\text{const.},\end{aligned} \tag{41}$$

where $\delta J=J-J_n$, and use has been made of the resonance condition in Eq. (38). It follows from Eq. (41) that the full width of the nth-order primary resonance is given by

$$\Delta J_n=\left[\frac{32|a_{n,-1}(J_n)|}{(\partial\omega_\beta/\partial J)_{J=J_n}}\right]^{1/2} \tag{42}$$

in the action variable, or equivalently by

$$\Delta r_n=\left(\frac{\partial r}{\partial J}\right)_{P_\theta,J=J_n}\Delta J_n \tag{43}$$

in the radial coordinate.

The procedure for evaluating the resonance width ΔJ_n in Eq. (42) is the following. First, to determine $(\partial\omega_\beta/\partial J)_{J=J_n}$ and associated quantities such as J_n, Eq. (38) is solved numerically in terms of outer turning point $r_n=r(J_n,\phi=0)\geqslant r_0$, using Newton's method. This gives the values of r_n, J_n, $H_0(r_n,P_\theta)$, $(\partial\omega_\beta/\partial r)_{r=r_n}$, etc. Using the chain rule for differentiation, this procedure also allows the numerical evaluation of $(\partial\omega_\beta/\partial J)_{J=J_n}$. Second, to determine the Fourier coefficient $a_{n,-1}(J_n)$, the Hamiltonian perturbation $H_1(J_n,\phi,s)$ is computed numerically on a two-dimensional mesh in the variables ϕ and s, where ϕ ranges from 0 to 2π and s ranges from 0 to S. A two-dimensional discrete Fourier transform is then used to evaluate the Fourier coefficient $a_{n,-1}(J_n)$, instead of the continuous representation in Eq. (36). Finally, the resonance width ΔJ_n (or corresponding resonance width Δr_n in radial coordinate r) is obtained by substituting the values of $a_{n,-1}(J_n)$ and $(\partial\omega_\beta/\partial J)_{J=J_n}$ into Eq. (42).

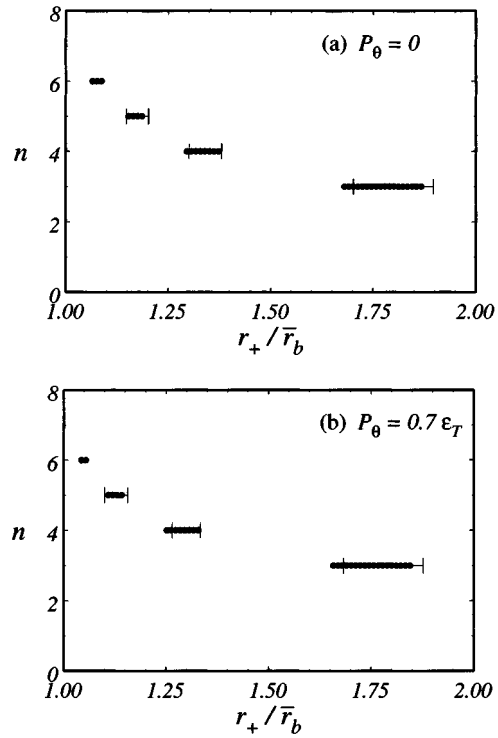

FIG. 5. Plots of the locations and full widths of the primary resonances of order $n=3-6$ obtained for the choices of system parameters corresponding to: (a) $\eta=0.2$, $\sigma_v=80°$ $(S^2\hat{\kappa}_z=8.712)$, $\sigma=26.2°$ $(SK/\varepsilon_T=3.8)$, $\omega_b=0$, and $P_\theta=0$; and (b) $\eta=0.2$, $\sigma_v=80°$ $(S^2\hat{\kappa}_z=8.712)$, $\sigma=26.2°$ $(SK/\varepsilon_T=3.8)$, $\omega_b=0$, and $P_\theta/\varepsilon_T=0.7$. The solid lines correspond to the analytical estimates given in Eq. (42), whereas the dotted lines are obtained by integrating Eq. (17) numerically.

Figure 5 shows plots of the locations and full widths of the primary resonances of order $n=3-6$ obtained for the choices of system parameters corresponding to: (a) $\eta=0.2$, $\sigma_v=80°$ $(S^2\hat{\kappa}_z=8.712)$, $\sigma=26.2°$ $(SK/\varepsilon_T=3.8)$, $\omega_b=0$, and $P_\theta=0$; and (b) $\eta=0.2$, $\sigma_v=80°$ $(S^2\hat{\kappa}_z=8.712)$, $\sigma=26.2°$ $(SK/\varepsilon_T=3.8)$, $\omega_b=0$, and $P_\theta/\varepsilon_T=0.7$. In Fig. 5, the solid lines correspond to the analytical estimates given in Eq. (43), whereas the dotted lines are obtained by integrating Eq. (17) numerically. For the lower-order primary nonlinear resonances with $n=3$, 4, and 5, the analytical estimates are in good agreement with the numerical results. For the sixth-order primary nonlinear resonance, however, we cannot obtain an analytical estimate of its width because numerical noise becomes sizable in computing the Fourier amplitude $a_{6,-1}$.

The nonlinear resonances for the cases presented in Figs. 5(a) and 5(b) are further illustrated with the Poincaré surface-of-section plots[21] shown in Figs. 6(a) and 6(b), respectively. Here, the Poincaré surface-of-section plots are generated by plotting the successive intersections of 15 test-particle trajectories, obtained from numerical integration of Eq. (17), with the phase space (r,P_r) at the lattice points

Downloaded 30 Aug 2001 to 192.55.106.156. Redistribution subject to AIP license or copyright, see http://ojps.aip.org/pop/popcr.jsp

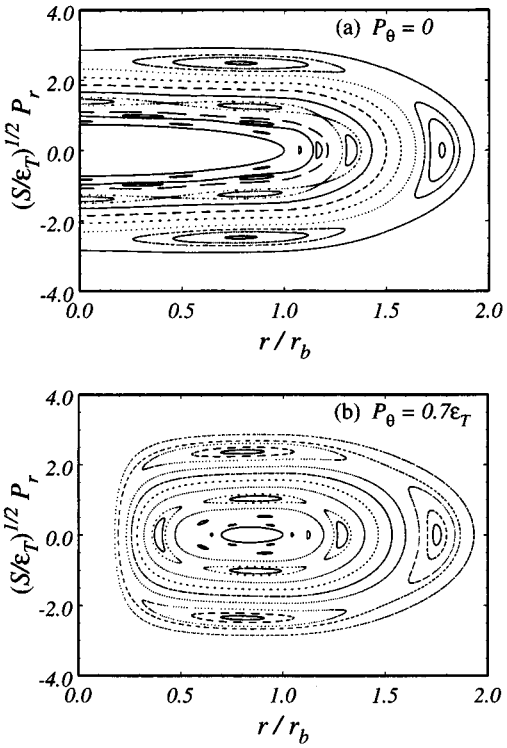

FIG. 6. Poincaré surface-of-section plots in the phase space (r,P_r) for 15 test particle trajectories moving through the periodic step-function lattice from $s/S=0$ to 1000 under the influence of the space-charge forces in a KV beam equilibrium. Here, the choices of systems parameters in (a) and (b) are the same as in Figs. 5(a) and 5(b), respectively.

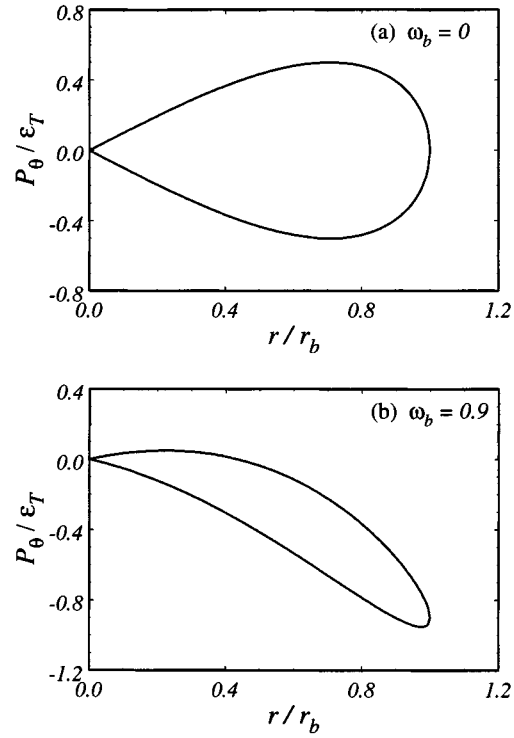

FIG. 7. Plots of the normalized canonical angular momentum P_θ/ε_T vs normalized radius r/r_b calculated from Eq. (45) for the choices of system parameters: (a) $\omega_b=0$ and (b) $\omega_b=0.9$.

$s=0,S,2S,\ldots,1000S$. Evidently, the locations and widths of the primary nonlinear resonances shown in Fig. 6 are in agreement with those shown in Fig. 5.

IV. PHASE SPACE STRUCTURE

In this section, use is made of the Poincaré surface-of-section method to examine the phase-space structure described by the Hamiltonian H in Eq. (18). Of particular interest are the nonlinear resonances and chaotic particle motion of test particles outside the boundary of the phase space occupied by the interior beam particles making up the rigid-rotor Vlasov equilibrium distribution f_0 (Refs. 23 and 24) in Eq. (A1). The phase-space boundary of the rigid-rotor Vlasov equilibrium is a closed surface in the three-dimensional phase space (r,P_r,P_θ) at any given axial distance s. A projection of such a boundary onto the phase space (r,P_θ) can be determined from

$$[\mathcal{H}_\perp+\omega_b P_\Theta-\tfrac{1}{2}(1-\omega_b^2)\varepsilon_T]_{P_R=0}=0, \tag{44}$$

where P_R, P_Θ, and $\mathcal{H}_\perp$ are defined in Eqs. (A4), (A5), and (A7), respectively. Substituting Eqs. (A2)–(A5) and (A7) into Eq. (44) yields

$$\left[\frac{P_\theta r_b(s)}{\varepsilon_T r}+\omega_b\frac{r}{r_b(s)}\right]^2=(1-\omega_b^2)\left[1-\frac{r^2}{r_b^2(s)}\right]. \tag{45}$$

Figure 7 shows plots of the normalized canonical angular momentum P_θ/ε_T versus normalized radius r/r_b described by Eq. (45) for the following choices of system parameters: (a) $\omega_b=0$ and (b) $\omega_b=0.9$. All of the interior beam particles in the equilibrium distribution are enclosed by such a loop shown in Fig. 7.

The phase-space structure for test particle motion is illustrated by the Poincaré surface-of-section plots shown in Figs. 8–10 for a wide range of system parameters. The Poincaré surface-of-section plots in Figs. 8–10 are generated by plotting the successive intersections of test-particle trajectories, obtained from numerical integration of Eq. (17), with the phase space (r,P_r) at the lattice points $s=0.5S$, $1.5S$, $2.5S$, etc.

Figure 8 shows Poincaré surface-of-section plots in the phase space (r,P_r) for 15 test particle trajectories moving through the periodic step-function lattice from $s/S=0.5$ to 1000.5 under the influence of the space-charge forces in a KV beam equilibrium. In Fig. 8, the choices of system parameters correspond to: (a) $\sigma_v=80°$, $\eta=0.2$, $\sigma=11.0°$ $(SK/\varepsilon_T=10)$, $\omega_b=0$, and $P_\theta/\varepsilon_T=0$; and (b) $\sigma_v=80°$, $\eta=0.2$, $\sigma=11.0°$ $(SK/\varepsilon_T=10)$, $\omega_b=0$, and $P_\theta/\varepsilon_T=0.45$. For both cases shown in Fig. 8, one test particle is initialized at the phase-space boundary of the KV equilibrium distribution, and the corresponding test-particle orbit is represented in Fig. 8(a) by the inner curved arc approaching $r/r_b=1$, and in Fig. 8(b) by the innermost contour extending from $r/r_b=0.54$ to 0.84. The remaining test particles are initialized outside the beam, i.e., outside the phase-space boundary of the KV equilibrium distribution. Some of these particles undergo chaotic motion. By comparing Fig. 8(a) with Fig. 8(b), it is evident that the phase-space structure changes significantly as the canonical angular momentum P_θ is varied. In particular, it is interesting to observe that there are many

Downloaded 30 Aug 2001 to 192.55.106.156. Redistribution subject to AIP license or copyright, see http://ojps.aip.org/pop/popcr.jsp

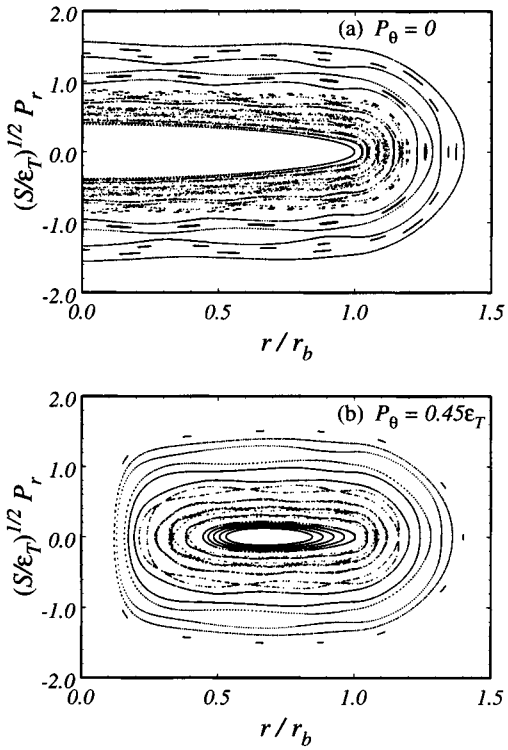

FIG. 8. Poincaré surface-of-section plots in the phase space (r,P_r) for 15 test particle trajectories moving through the periodic step-function lattice from $s/S=0.5$ to 1000.5 under the influence of the space-charge forces in a KV beam equilibrium. Here, the choices of system parameters correspond to: (a) $\sigma_v=80°$, $\eta=0.2$, $\sigma=11.0°$ $(SK/\varepsilon_T=10)$, $\omega_b=0$, and $P_\theta/\varepsilon_T=0$; and (b) $\sigma_v=80°$, $\eta=0.2$, $\sigma=11.0°$ $(SK/\varepsilon_T=10)$, $\omega_b=0$, and $P_\theta/\varepsilon_T=0.45$.

nonlinear resonances and chaotic regions in the vicinity of the phase-space boundary of the KV equilibrium distribution for the case shown in Fig. 8(a) $(P_\theta=0)$, whereas the nonlinear resonances and chaotic regions are well separated, by a dense set of invariant curves, i.e., KAM surfaces,[21] from the phase-space boundary of the KV equilibrium distribution for the case shown in Fig. 8(b) $(P_\theta/\varepsilon_T=0.45)$. In general, as the canonical angular momentum P_θ increases in magnitude, the nonlinear resonances and chaotic regions move further away from the phase-space boundary of the KV equilibrium distribution. Consequently, for a KV equilibrium, particles with $P_\theta=0$ are the most likely to escape from the beam interior to enter into chaotic regions in phase space, forming a halo.

The Poincaré surface-of-section plots in Fig. 9 illustrate how the phase-space structure varies as the beam intensity, measured by the normalized parameter SK/ε_T, is increased. The choices of system parameters in Fig. 9 correspond to $\sigma_v=80°$, $\eta=0.2$, $\omega_b=0$, and $P_\theta/\varepsilon_T=0$ at the following normalized beam intensities: (a) $SK/\varepsilon_T=0.5$ $(\sigma=66.8°)$, (b) $SK/\varepsilon_T=1.0$ $(\sigma=56.3°)$, (c) $SK/\varepsilon_T=3.0$ $(\sigma=31.5°)$, and (d) $SK/\varepsilon_T=7.0$ $(\sigma=15.4°)$. For the low-intensity case shown in Fig. 9(a), the phase space is almost entirely regular. For the moderate-intensity cases shown in Figs. 9(b) and 9(c), nonlinear resonances appear. The most pronounced among these resonances is the third-order primary nonlinear resonance. As the beam intensity is further increased, the widths of higher-order nonlinear resonances increase, which is evident from Fig. 9(d). In general, the nonlinear resonances and chaotic regions increase in size as the beam intensity is increased.

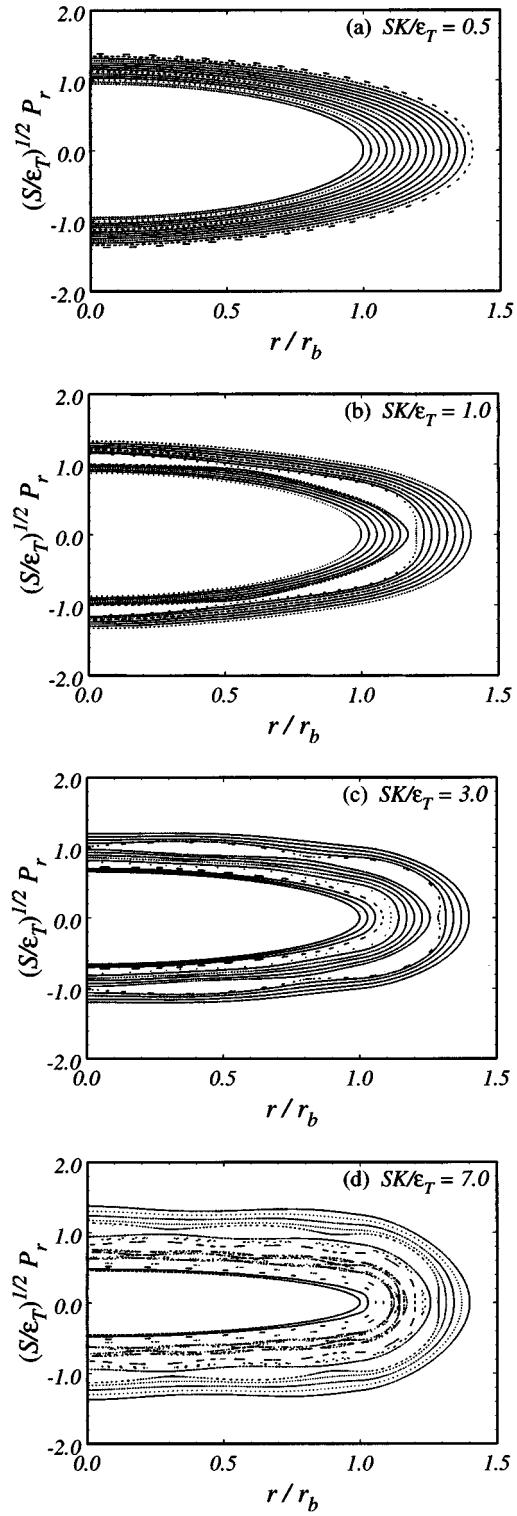

FIG. 9. Poincaré surface-of-section plots in the phase space (r,P_r) for 15 test particle trajectories moving through the periodic step-function lattice from $s/S=0.5$ to 1000.5 under the influence of the space-charge forces in a KV beam equilibrium at several beam intensities. Here, the choices of systems parameters correspond to $\sigma_v=80°$, $\eta=0.2$, $\omega_b=0$, and $P_\theta/\varepsilon_T=0$ at the following normalized beam intensities: (a) $SK/\varepsilon_T=0.5$ $(\sigma=66.8°)$, (b) $SK/\varepsilon_T=1.0$ $(\sigma=56.3°)$, (c) $SK/\varepsilon_T=3.0$ $(\sigma=31.5°)$, and (d) $SK/\varepsilon_T=7.0$ $(\sigma=15.4°)$.

Downloaded 30 Aug 2001 to 192.55.106.156. Redistribution subject to AIP license or copyright, see http://ojps.aip.org/pop/popcr.jsp

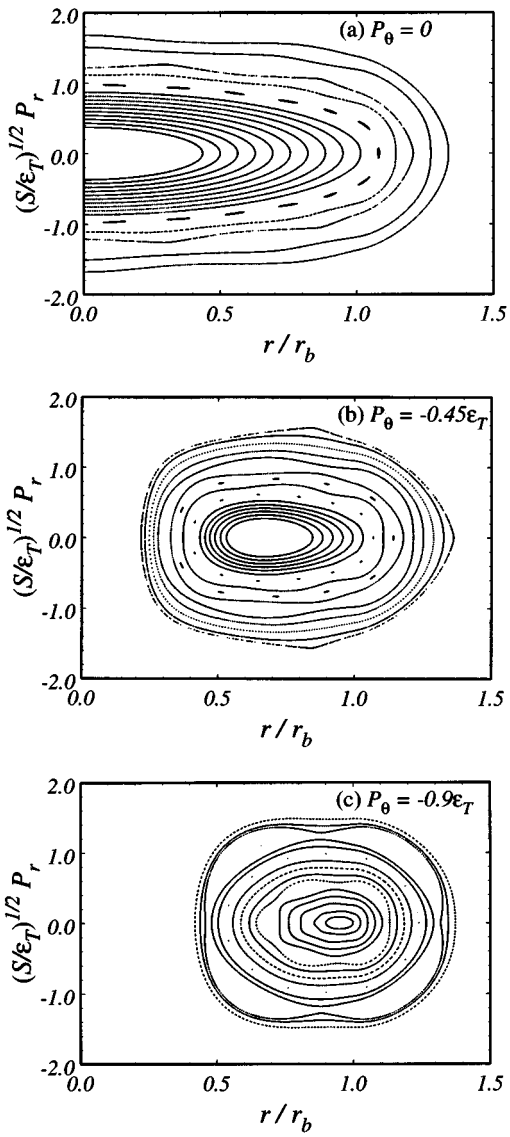

FIG. 10. Poincaré surface-of-section plots in the phase space (r,P_r) for 15 test particle trajectories moving through the periodic step-function lattice from $s/S=0.5$ to 1000.5 under the influence of the space-charge forces in a rigid-rotor Vlasov equilibrium. Here, the choices of system parameters correspond to: $\sigma_v=80°$, $\eta=0.2$, $\sigma=11.0°$ $(SK/\varepsilon_T=10)$, $\omega_b=0.9$, and (a) $P_\theta/\varepsilon_T=0$, (b) $P_\theta/\varepsilon_T=-0.45$, and (c) $P_\theta/\varepsilon_T=-0.9$.

The influence of beam rotation $(\omega_b\neq 0)$ on the phase-space structure is illustrated by the Poincaré surface-of-section plots shown in Fig. 10. The choices of system parameters in Fig. 10 correspond to: $\sigma_v=80°$, $\eta=0.2$, $\sigma=11.0°$ $(SK/\varepsilon_T=10)$, $\omega_b=0.9$, and (a) $P_\theta/\varepsilon_T=0$, (b) $P_\theta/\varepsilon_T=-0.45$, and (c) $P_\theta/\varepsilon_T=-0.9$. For all three cases shown in Fig. 10, the innermost orbit corresponds to a test particle that is initialized at the phase space boundary of the rigid-rotor Vlasov equilibrium. By comparing Fig. 10 with Fig. 8 for the KV distribution where the beam rotation is absent $(\omega_b=0)$, we find that the presence of beam rotation tends to reduce the degree of chaotic behavior in phase space. This is evident when we compare Fig. 10(c) with Fig. 8(a). For both cases shown in Fig. 10(c) and Fig. 8(a), the value of P_θ is chosen such that the boundary of the equilibrium distribution extends to $r=r_b$ [see Fig. 7 or Eq. (45)].

Finally, we discuss the implications of the rich nonlinear resonance structure and chaotic particle motion for beam halo formation. Based on a comprehensive study of the phase-space structure for test-particle motion for vacuum phase advance $\sigma_v=80°$, we have shown that the phase-space structure is almost entirely regular at low beam intensity (phase advance $\sigma\gtrsim 70°$, say), whereas at moderate beam intensity $(30°\lesssim\sigma\lesssim 70°)$, nonlinear resonances appear, the most pronounced of which is the third-order primary nonlinear resonance. As the beam intensity is further increased $(\sigma\lesssim 30°)$, the widths of the higher-order nonlinear resonances increase, and the chaotic region of phase space increases in size. Furthermore, the many chaotic layers associated with the separatrices of the primary and secondary nonlinear resonances are still divided by the remaining invariant KAM surfaces, even at very high beam intensities. Therefore, in the context of the present test-particle analysis, chaotic layers do *not* form an extended chaotic region in phase space. In actual beam propagation experiments, however, it is expected that sufficient beam mismatch or perturbations about the periodically focused beam equilibrium can cause the particles to cross the invariant surfaces and form a halo.

V. CONCLUSIONS

Test particle motion has been analyzed analytically and numerically in the field configuration consisting of the equilibrium self-electric and self-magnetic fields of a thin, continuous, intense charged-particle beam and an applied periodic focusing solenoidal magnetic field. In the present analysis, the self fields were determined self-consistently, assuming the beam to have a rigid-rotor Vlasov equilibrium distribution. The canonical equations of motion for individual test particles were derived from a Hamiltonian. Using the Hamilton–Jacobi method, the betatron oscillations of test particles in the average self fields and applied field were analyzed, and the nonlinear resonances induced by periodic modulations in the self fields and applied field were determined. Analytical estimates of the locations and widths of the primary nonlinear resonances were found to be in good agreement with Poincaré surface-of-section plots obtained by integrating numerically the equations of motion.

Use was made of the Poincaré surface-of-section method to analyze the phase-space structure for test particle motion outside the outermost envelope of the beam over a wide range of system parameters. It was found that the phase-space structure changes significantly as the canonical angular momentum (P_θ), beam intensity (as measured by SK/ε_T or σ/σ_v), vacuum phase advance σ_v, or beam rotation (ω_b) is varied. For an intense beam with KV equilibrium distribution $(\omega_b=0)$, it was shown that the chaotic regions approach the phase-space boundary of the equilibrium distribution as the canonical angular momentum P_θ decreases in magnitude. Consequently, when there are perturbations about the equilibrium, particles with zero canonical angular momentum are the most likely to escape from the beam interior to enter into the chaotic regions, forming a halo. The phase-space structure was also analyzed for test-particle motion under the in-

Downloaded 30 Aug 2001 to 192.55.106.156. Redistribution subject to AIP license or copyright, see http://ojps.aip.org/pop/popcr.jsp

fluence of the self fields of an intense beam with a rigid-rotor Vlasov equilibrium distribution ($\omega_b \neq 0$). It was found that the presence of beam rotation reduces the degree of chaotic behavior in phase space.

For $\sigma_v < 80°$, the test-particle analysis showed that at very high beam intensities, the chaotic layers associated the separatrices of nonlinear resonances are still divided by the remaining invariant KAM surfaces and do not overlap completely to form an extended chaotic region. Although the chaotic layers do not form an extended chaotic region in the context of present test-particle analysis, any sizable beam mismatch or perturbations about the periodically-focused beam equilibrium may cause particles to cross the invariant surfaces, thereby resulting in a halo.

ACKNOWLEDGMENTS

This research was supported by Department of Energy under Grant No. DE-FG02-95ER-40919 and Contract No. DE-AC02-76-CH0-3073, and by Air Force Office of Scientific Research under Grant No. F49620-97-1-0325. The research by R.P. was also supported by CAPES, Brazil.

APPENDIX: RIGID-ROTOR VLASOV EQUILIBRIUM

The transverse phase-space distribution that self-consistently generates the density profile in Eq. (3) is given by the rigid-rotor Vlasov equilibrium distribution function[23,24]

$$f_b^0(R,P_R,P_\Theta)=\frac{N_b}{2\pi^2\varepsilon_T}\delta\left[\mathcal{H}_\perp+\omega_b P_\Theta-\frac{1}{2}(1-\omega_b^2)\varepsilon_T\right]. \tag{A1}$$

In Eq. (A1), $\omega_b=\text{const.}$ $(-1<\omega_b<1)$ is a parameter measuring beam rotation relative to the Larmor frame. The normalized canonical phase-space variables (R,Θ,P_R,P_Θ) are related to the Larmor-frame phase-space variables $(\tilde{r},\tilde{\theta},\tilde{P}_r,\tilde{P}_\theta)$ by

$$R=\frac{\sqrt{\varepsilon_T}}{r_b(s)}\tilde{r}, \tag{A2}$$

$$\Theta=\tilde{\theta}, \tag{A3}$$

$$P_R=\frac{1}{\sqrt{\varepsilon_T}}\left[r_b(s)\frac{d}{ds}\tilde{r}-\tilde{r}\frac{d}{ds}r_b(s)\right], \tag{A4}$$

$$P_\Theta=\tilde{P}_\theta, \tag{A5}$$

through the generating function

$$F_2(\tilde{r},\tilde{\theta},P_R,P_\Theta,s)=\frac{\sqrt{\varepsilon_T}}{r_b(s)}\tilde{r}P_R+\tilde{\theta}P_\Theta+\frac{\tilde{r}^2}{r_b(s)}\frac{d}{ds}r_b(s). \tag{A6}$$

The effective transverse Hamiltonian $\mathcal{H}_\perp$ occurring in Eq. (A1) is defined for $R<\sqrt{\varepsilon_T}$ (or equivalently for $\tilde{r}<r_b$) by

$$\mathcal{H}_\perp(R,P_R,P_\Theta)=\frac{r_b^2(s)}{\varepsilon_T}\left[H_\perp(R,P_R,P_\Theta,s)-\frac{K}{2}-K\ln\frac{r_w}{r_b(s)}\right]$$
$$=\frac{1}{2}\left(P_R^2+\frac{P_\Theta^2}{R^2}+R^2\right), \tag{A7}$$

where $H_\perp(R,\Theta,P_R,P_\Theta,s)=\tilde{H}_\perp(\tilde{r},\tilde{P}_r,\tilde{P}_\theta,s)+\partial F_2/\partial s$ is the Hamiltonian expressed in the canonical variables (R,Θ,P_R,P_Θ).

For a particle moving in the beam interior ($R<\sqrt{\varepsilon_T}$ or equivalently $\tilde{r}<r_b$), it follows from the Hamilton equations of motion, $dR/ds=\partial H_\perp/\partial P_R$, $d\Theta/ds=\partial H_\perp/\partial P_\Theta$, $dP_R/ds=-\partial H_\perp/\partial R$, and $dP_\Theta/ds=-\partial H_\perp/\partial\Theta=0$, that the effective transverse energy $\mathcal{H}_\perp$ is a constant of the motion, although the transverse Hamiltonian $H_\perp$, in general, is not a constant of the motion. Because $H_\perp$ is independent of Θ, the canonical angular momentum P_Θ is also a constant of the motion, in agreement with Eqs. (16) and (A5). Therefore, the equilibrium distribution function f_b^0 satisfies exactly the steady-state nonlinear Vlasov equation

$$\frac{\partial f_b^0}{\partial s}+\frac{\partial H_\perp}{\partial P_R}\frac{\partial f_b^0}{\partial R}-\frac{\partial H_\perp}{\partial R}\frac{\partial f_b^0}{\partial P_R}=0 \tag{A8}$$

with $\partial f_b^0/\partial s=0$. Making use of $\int dx'\,dy'\cdots=[\varepsilon_T/r_b^2(s)R]\int dP_R dP_\Theta\cdots$, it is readily shown that $n_b(r,s)=\int dx'\,dy' f_b^0$ is indeed identical to the step-function density profile defined in Eq. (3).

[1] *Space Charge Dominated Beams and Applications of High Brightness Beams*, edited by S. Y. Lee [AIP Conf. Proc. **377** (1996)], and references therein.
[2] I. Haber, D. Kehne, M. Reiser, and H. Rudd, Phys. Rev. A **44**, 5194 (1991).
[3] J. S. O'Connell, T. P. Wangler, R. S. Mills, and K. R. Crandall, *Proceedings of the 1993 Particle Accelerator Conference* (IEEE, Piscataway, NJ, 1993), Vol. 5, p. 3657.
[4] C. Chen and R. C. Davidson, Phys. Rev. Lett. **72**, 2195 (1994); Phys. Rev. E **49**, 5679 (1994).
[5] Q. Qian, R. C. Davidson, and C. Chen, Phys. Plasmas **1**, 3104 (1994).
[6] R. L. Gluckstern, Phys. Rev. Lett. **73**, 1247 (1994).
[7] T. Chen, J. Irwin, and R. Siemann, Phys. Rev. E **49**, 2323 (1994).
[8] L. M. Lagniel, Nucl. Instrum. Methods Phys. Res. A **345**, 1576 (1995); Proceedings of the Fifth European Particle Accelerator Conference, 1996 (unpublished), p. 163.
[9] Q. Qian, R. C. Davidson, and C. Chen, Phys. Plasmas **2**, 2674 (1995).
[10] C. Chen and R. A. Jameson, Phys. Rev. E **52**, 3074 (1995).
[11] S. Y. Lee and A. Riabko, Phys. Rev. E **51**, 1609 (1995); A. Riabko *et al.*, *ibid.* **51**, 3529 (1995).
[12] I. Haber, D. A. Callahan, A. Friedman, D. P. Grote, D. Kehne, A. B. Langdon, M. Reiser, H. Rudd, H. Suk, D. X. Wang, and J. G. Wang, in Ref. 1, p. 105.
[13] F. L. Krawczyk, J. H. Billen, R. D. Ryne, H. Takeda, and L. M. Young, in *Proceedings of the 1995 Particle Accelerator Conference* (IEEE, Piscataway, NJ, 1995), p. 2306, and references therein.
[14] S. Yu, S. Eylon, E. Henestroza, and D. Grote, in Ref. 1, p. 134.
[15] C. Chen, Y. Fink, R. C. Davidson, and Q. Qian, *Proceedings of the 11th International Conference on High Power Particle Beams* (Institute of Plasma Physics, Academy of Sciences of the Czech Republic, 1996), p. 1018.
[16] Y. Fink, C. Chen, and W. P. Marable, Phys. Rev. E **55**, 7557 (1997).
[17] M. Pabst, K. Bongardt, and A. P. Letchford, in Ref. 1, p. 343.
[18] R. W. Garnett, J. H. Billen, K. C. D. Chan, R. Genzlinger, E. R. Gray, S. Nath, R. Rusnak, D. L. Schrage, J. E. Stovall, H. Takeda, R. Wood, T. P. Wangler, and L. M. Young, in Ref. 1, p. 60.
[19] R. Pakter and C. Chen, *Proceedings of 1997 Particle Accelerator Conference* (IEEE, Piscataway, NJ, 1997), p. 1938.

Downloaded 30 Aug 2001 to 192.55.106.156. Redistribution subject to AIP license or copyright, see http://ojps.aip.org/pop/popcr.jsp

[20] H. Okamoto and M. Ikegami, Phys. Rev. E **55**, 4694 (1997).
[21] A. J. Lichtenberg and M. A. Lieberman, *Regular and Chaotic Dynamics*, 2nd ed. (Springer, New York, 1992).
[22] R. C. Davidson, *Physics of Nonneutral Plasmas* (Addison–Wesley, Reading, MA, 1990).
[23] C. Chen, R. Pakter, and R. C. Davidson, Phys. Rev. Lett. **79**, 225 (1997).
[24] R. C. Davidson and C. Chen, Part. Accel. **59**, 175 (1998).
[25] I. M. Kapchinskij and V. V. Vladimirskij, in *Proceedings of the International Conference on High Energy Accelerators* [European Laboratory for Particle Physics (CERN), Geneva, 1959], p. 274.
[26] M. Reiser, *Theory and Design of Charged-Particle Beams* (Wiley, New York, 1994).
[27] H. Goldstein, *Classical Mechanics*, 2nd ed. (Addison-Wesley, Reading, MA, 1981).

Downloaded 30 Aug 2001 to 192.55.106.156. Redistribution subject to AIP license or copyright, see http://ojps.aip.org/pop/popcr.jsp